STScI | SPACE TELESCOPE SCIENCE INSTITUTE

JWST ANALYSIS REPORT

Title: NAP-018: NIS-018 NIRISS GR700XD Wavelength Calibration (NGAS CAR-702, APT 1092)	Doc #: JWST-STScI-008422, SM-09 Date: 16 Mar 2023 Rev: -
Authors: Joseph Filippazzo, Arpita Roy Phone:410-338-6871	Release Date: 17 April 2023

1. Abstract

We present the analysis plan for the commissioning activity NIS-018, NIRISS GR700XD Wavelength Calibration (NGAS CAR-702, APT 1092). The goal of this program was to obtain and analyze observations taken with the GR700XD grism in order to derive nominal wavelength values for spectral orders 1, 2, and 3 at each pixel in the SUBSTRIP256 subarray on the NIRISS detector. The 1D wavelength values were successfully derived for all orders in the analysis by identifying the pixel locations of absorption features in observations of A, F, and M dwarf stars taken during commissioning. A 2D wavelength map for each order was then produced as a reference file for the JWST data reduction pipeline.

2. Introduction

In this commissioning activity, the wavelength dispersion solution of the GR700XD grism — used in the Single Object Slitless Spectroscopy (SOSS) mode of NIRISS — was derived using the absorption features of a late M-type main sequence star, an F-type star, and an A-type star. The relation between the relative pixel positions and the wavelengths of the absorption features was computed and mapped for all three spectral orders present in this mode. The quantities derived from these observations serve as inputs to the spectral analysis software tools developed to extract and calibrate the GR700XD spectra.

A late-type M dwarf was selected as the target for this program given its strong atomic and molecular absorption features at red optical as well as near-infrared wavelengths. While a more photometrically stable A star was preferable for the photometric calibration program (NIS-017, APT 1091), its strongest absorption features are those of hydrogen. This does not provide a dense enough set of anchor points for accurate wavelength calibration in the 0.6 – 2.8μm range observed in SOSS mode.

Initially we produced a 2D SOSS simulation by scaling the traces observed during CV3 tests to the flux of ground based target data, which could then be used to calibrate the M-dwarf spectra observed by NIRISS. However, it was found that distortion and other subtle optical changes in flight (e.g. the effective input focal ratio) were causing differences between the CV3-based simulation and observation that were impeding sub-pixel calibration precision. We thus switched to a simpler and broader approach, that of directly calibrating the lines and features observed in

NIS-017, NIS-018, and NIS-034, and forging a joint solution. For the A and F stars in NIS-017 and NIS-034 respectively, we fit the pixel positions of the hydrogen lines and assigned them to known wavelengths. For the M-dwarf we used adaptive windows to measure the features against a BT-Settl (Allard et al. 2012) model atmosphere (T_{eff}=3200, log(g)=4.5, [Fe/H]=0.0) that was convolved down to the SOSS resolution and sampling. This yielded absolute wavelength vs. pixel values for each of the three stars, which were then fit jointly with a low-order polynomial to independently produce wavelength calibration results for SOSS orders 1, 2, and 3.

Potential targets were chosen by spectral type and apparent magnitude so as to reduce the risk of detector saturation. Since the observations of this program are scheduled in the cold attitude (L+137 days to L+145 days and -45° <= pitch <= - 35°), only stars encompassed by the JWST sky visibility annulus at this pitch angle as it slides along the ecliptic over this 2-week period are valid targets. Three of the four main sequence late M-type stars in the annulus suffer from significant spectral contamination from neighbors over a wide range of PAs that severely limit their visibility. The best M-type candidate was thus TWA 33 of spectral type M5.5e and 2MASS K_s = 9.1. The F-type star used in this analysis, HAT-P-14 (type F5V, K_s = 8.851), was observed for the NIS-034 NIRISS Sensitivity and Stability for Transiting Exoplanet Observations commissioning program. The A-type star used in this analysis, BD+60°1753 (type A0mA1V, K_s = 9.645), was observed for the NIS-017 GR700XD Photometric Calibration commissioning program. Selection criteria and observing strategies for the A and F stars are described in the JWST Analysis Reports for the NIS-017 (JWST-STScI-008270, SM-12) and NIS-034 (in prep) commissioning programs, respectively.

3. Data and Simulations

The exposures for this activity were collected in two observations. In the first observation, the star was observed in the two science subarrays of the SOSS mode: SUBSTRIP96 and SUBSTRIP256, to measure the light loss between these subarrays as a function of detector spatial dimension. As in the ground tests, exposures with the GR700XD + F277W combination were included to isolate the red end of the 1st-order spectrum from contamination by the second order trace.

The first observation also included a short (0.5 hour), full-frame exposure of several short integrations. This exposure was useful and necessary for several secondary analysis objectives (not discussed in detail here):

(a) A direct comparison of the background in the full-frame and subarray exposures helped characterize the 1/f noise and its impact on a time series.

(b) The 4-amplifier readout introduces cross-talk from hot pixels in the full-frame. We assessed the impact of the cross-talk by comparing the integrated flux on the same star in these two readout configurations.

(c) The full-frame has the potential to allow a measurement of the loss of flux in the subarrays, i.e., the aperture correction. The SUBSTRIP256 subarray cuts into the wing of the trace so a small amount of flux is not measured. With this full-frame exposure, we can directly quantify this loss. However, the full frame observations taken for this program had too many contaminant traces from nearby sources to measure the aperture loss.

(d) The GR700XD + FULL frame is a supported configuration for SOSS mode so we exercised and characterized it ahead of user requests to deploy the mode. In the second observation, an offset in the spatial direction was applied to place the target trace near the center

of the detector. Short full-frame exposures were taken to characterize the background at the location of the science subarrays and to accurately measure the wavelength-dependent cross-dispersion profile of the traces.

The observations described above needed to be executed twice due to an issue with target acquisition in the first attempt. Ultimately, both these observations gave consistent results except for a few pixel offset induced by the change in the placement of the star on the detector between the first and second attempts.

The observations of NIS-018 complement those of program 1091 (NIS-017) and program 1541 (NIS-034) and offer a diversity of spectral types for the wavelength calibration, e.g., M-type in the red (this program) and F-type (1541) and A-type (1091) in the blue. The spectra of these stellar types have been well-studied in the red-optical and NIR with high-resolution instruments from the ground, e.g. Cushing et al. (2005) — using IRTF SpeX and Subaru IRCS; Rayner et al. (2009) — using IRTF SpeX, Reiners et al. (2018) — using Carmenes.

4. Analysis Steps

Prior to commissioning, a library of simulated 'template' spectra were prepared as wavelength calibrations for the observational data. These template spectra were produced with *mirage* (Multi-Instrument RAmp GEnerator) using both PHOENIX-ACES models and ground-based high-resolution observations from the SPIRou spectrograph at CFHT. This provided a test for mismatches between stellar atmosphere models and observations, as well as mismatches between ground and space based spectroscopy due to telluric contamination, unreliable absolute flux levels in stabilized fiber-fed spectrographs, and other instrumental effects.

During commissioning preparation, we found that using individual spectral lines works well for the A-star and F-star spectra, but was not feasible for M dwarfs with heavily blended forests of lines, particularly at R~700. Instead, we focused on molecular bandheads and other features that span multiple resolution elements (or "chunks") for the cooler and redder calibration target. Thus, along with the template spectra, we prepared corresponding chunk lists based on known lines, as well as empirical features observed in late-M stars.

4.1. Data Verification and Processing

As the observations were completed, we verified the completeness of the archived products in MAST and the accuracy of the basic FITS header keywords, as described in Martel (2019). We used Level 1 processing of the JWST calibration pipeline to calibrate raw exposures (_uncal.fits) to 4D corrected ramps (_0_rampfitstep.fits). Specifically, we applied the DQInitStep, SaturationStep, SuperBiasStep, RefPixStep, LinearityStep, DarkCurrentStep, JumpStep, and RampFitStep pipeline steps to the raw data and checked the outputs at each step. The primary pipeline products for the analysis are the raw count rate images for the SUBSTRIP96, SUBSTRIP256, and full frame cases.

While Level 2 products are available in MAST, we further processed the data with custom code to verify the fidelity of the results. The data were 1/f noise corrected on a column by column basis by subtracting the median value of the background pixels outside a 30 pixel radius from the trace centers. Figure 1 shows how this correction isolated the 1/f noise and allowed it to be subtracted from the target signal.

A custom trace finding algorithm was employed to isolate the pixels containing the target's order 1, 2, and 3 signals. The *transitspectroscopy* package[1] (Espinoza, 2022), which uses flux-weighted centroiding with a Gaussian filter to find the center of each trace order in the cross-dispersion direction in each detector column, was used. An aperture radius of 20 pixels was used for the order 1 trace and an aperture radius of 15 pixels was used for order 2 and order 3. The trace positions were then compared to those found from CV3 data to check consistency. While the location of the traces on the detector were fairly consistent, the commissioning data showed a slightly smaller radius of curvature on the blue ends of the traces than the CV3 data.

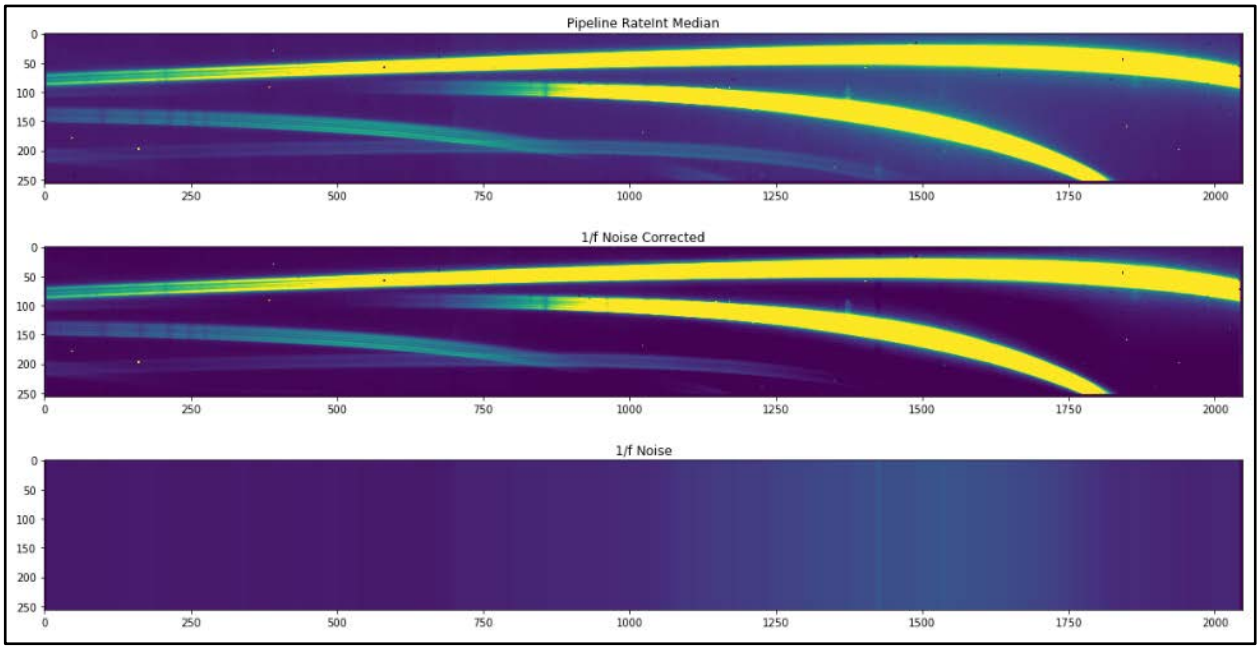

Figure 1. The raw (top), corrected (middle), and isolated 1/f noise (bottom) components of a median frame of NIS-018 data.

At the time of writing, the 1D extraction algorithm provided by the JWST pipeline for SOSS mode was not sufficiently robust for commissioning, hence we performed all spectral extraction with custom code from the *transitspectroscopy* package. Using the extraction apertures determined by the trace finding algorithm for each order, the total ADU/s in the signal pixels were added up. Then the background, defined as the the median of the pixels between the aperture radius and a background radius — 50 pixels for order 1 and 30 pixels for order 2 and order 3 — was subtracted to obtain the total signal in each column.

To better measure the spectral features in the data, continuum normalization of the extracted spectra was performed. The goal was to remove the spectral continuum so that the observed spectrum can be compared directly to the template without issues of flux calibration and instrument throughput modeling. While this continuum fit is not really taking out the "continuum", it performs similarly on both the template and the observation. A Savitzky-Golay filter, which uses local least-squares fitting of data by polynomials to smooth a spectrum, was applied to the spectra in 100 20-column chunks and then a cubic spline was fit to the curve to determine the shape of the pseudo-continuum to be removed. An extracted first order spectrum of the A-star along with the cubic spline fit and continuum normalized spectrum are shown in Figure 2.

[1] https://github.com/nespinoza/transitspectroscopy

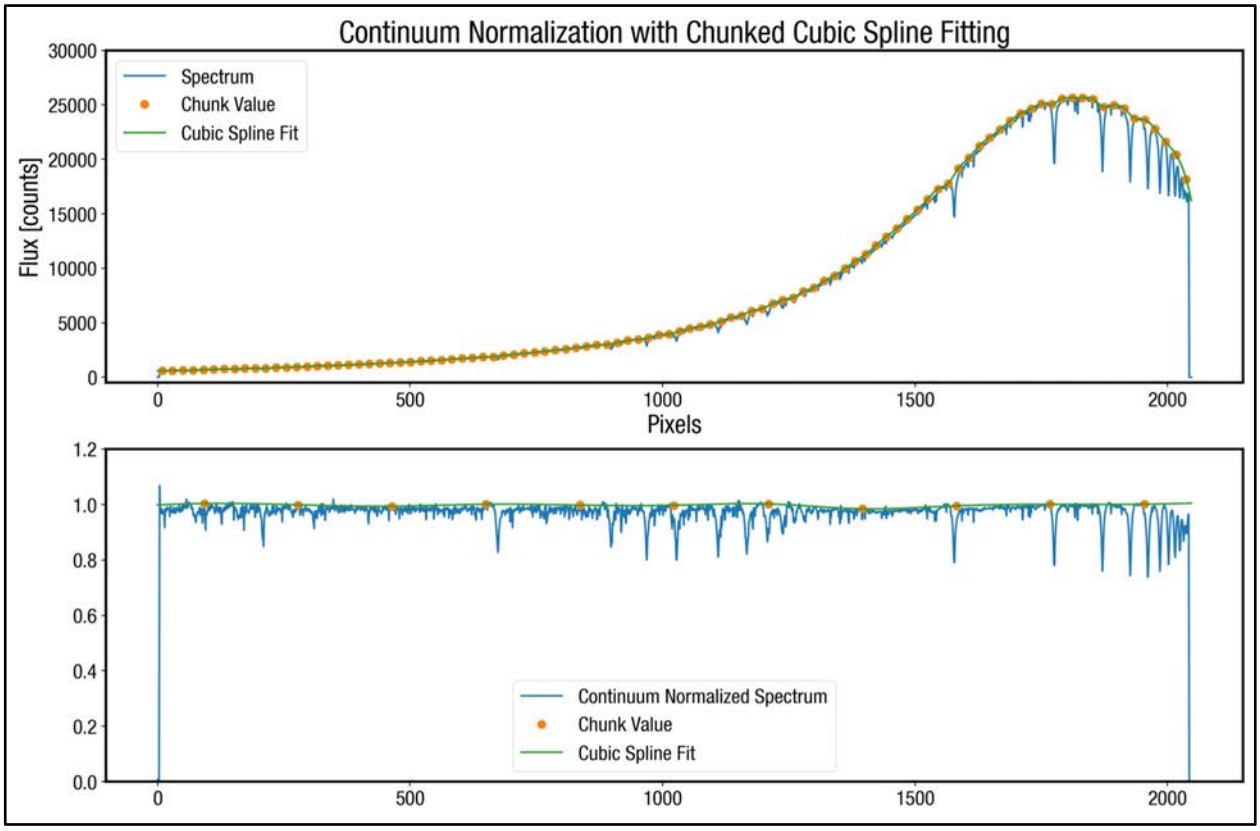

Figure 2. An example of an extracted order 1 countrate spectrum in ADU/s from a frame of A star data showing the counts as a function of detector column for order 1 (blue line), the measured continuum in each of 100 chunks (orange circles), and the best fit continuum (green line).

4.2. Wavelength Calibration

The first step of the wavelength calibration was a coarse check for multi-pixel offsets. This was done by performing an aperture extraction of the spectra and plotting them with the locations of the atomic and molecular features. We then examined the strongest absorption features to see if there were any large discrepancies between their x-positions and those of the theoretical vacuum wavelengths. Many appeared to be in good agreement but several showed offsets of up to 4 pixels or were too ambiguous given the complicated morphology of the M dwarf data.

To find the pixel locations of the strongest A and F star absorption features, a list of 340 hydrogen lines at vacuum wavelengths was first compiled using the Rydberg formula. After selecting those lines within the 0.6 – 2.8 μm range covered by SOSS mode that were also strong enough to identify by eye in the continuum corrected spectra of the A and F stars, we were left with 25 hydrogen lines to use as anchor points for the wavelength solution. Radial velocities for the A star (25.46 km/s) and F star (20.417 km/s) from Gaia EDR3 introduced negligible wavelength shifts to the observed spectra.

The detector x-positions of the 25 lines were identified for both the A star and F star by performing a least squares fit of a Gaussian to the data at each absorption feature. A non-linear offset was observed between the measured line locations of the A and F stars of as much as 1.75 pixels, shown in Figure 3. Overall, the A star lines appear to be shifted more to the right on the detector than those same lines in the F star, though they converge most around detector column

1250. This effect is under investigation though a joint wavelength solution within specifications was able to be achieved with the data in hand. The radial velocity difference between the A and F stars is only ~5km/s which translates into a relative shift on the order of 0.0001 pixels, an almost imperceptible shift which can be ruled out as the source of the wavelength discrepancy.

For the M-dwarf TWA-33, we used adaptive windows to measure the features against a BT-Settl (Allard, 2014) model atmosphere (T=3200K, log(g)=4.5, [Fe/H]=0.0) that was convolved down to SOSS resolution of 700. Since resolving power and dispersion are not constant across the bandpass, we treated the model atmosphere in 76 small — sometimes overlapping — chunks of 30 pixels each where these quantities vary imperceptibly. The values of resolving power and dispersion were estimated for each chunk from CV3 expectations. These were close enough to in-flight conditions to predict the average behavior across tens of pixels. The broad spectral chunks were cross correlated with the model atmosphere to determine the pixel shifts of each feature. A sample of these fits is shown in Figure 4.

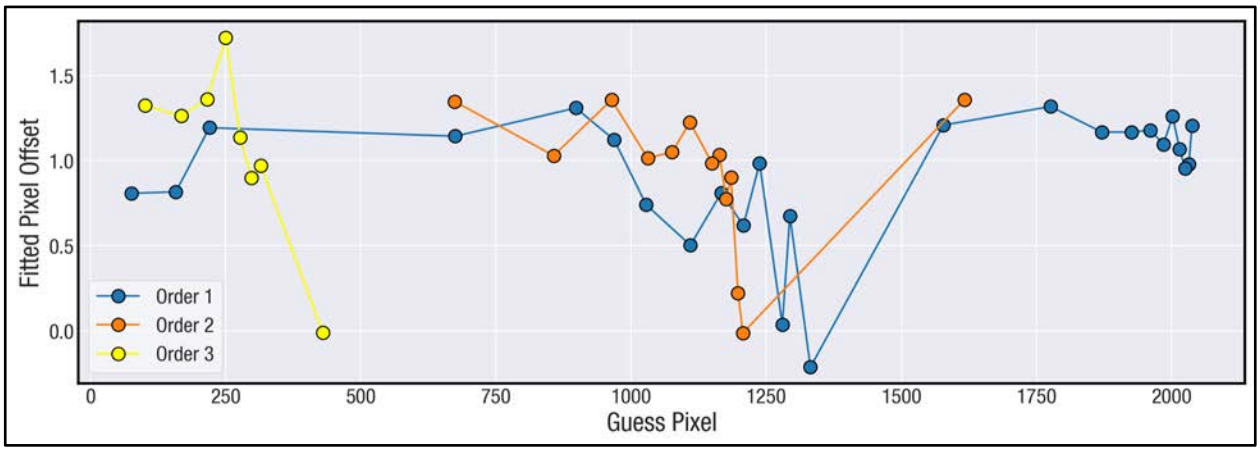

Figure 3. The offset between the A-star and F-star fitted pixel positions of each absorption feature for order 1 (blue), order 2 (orange) and order 3 (yellow).

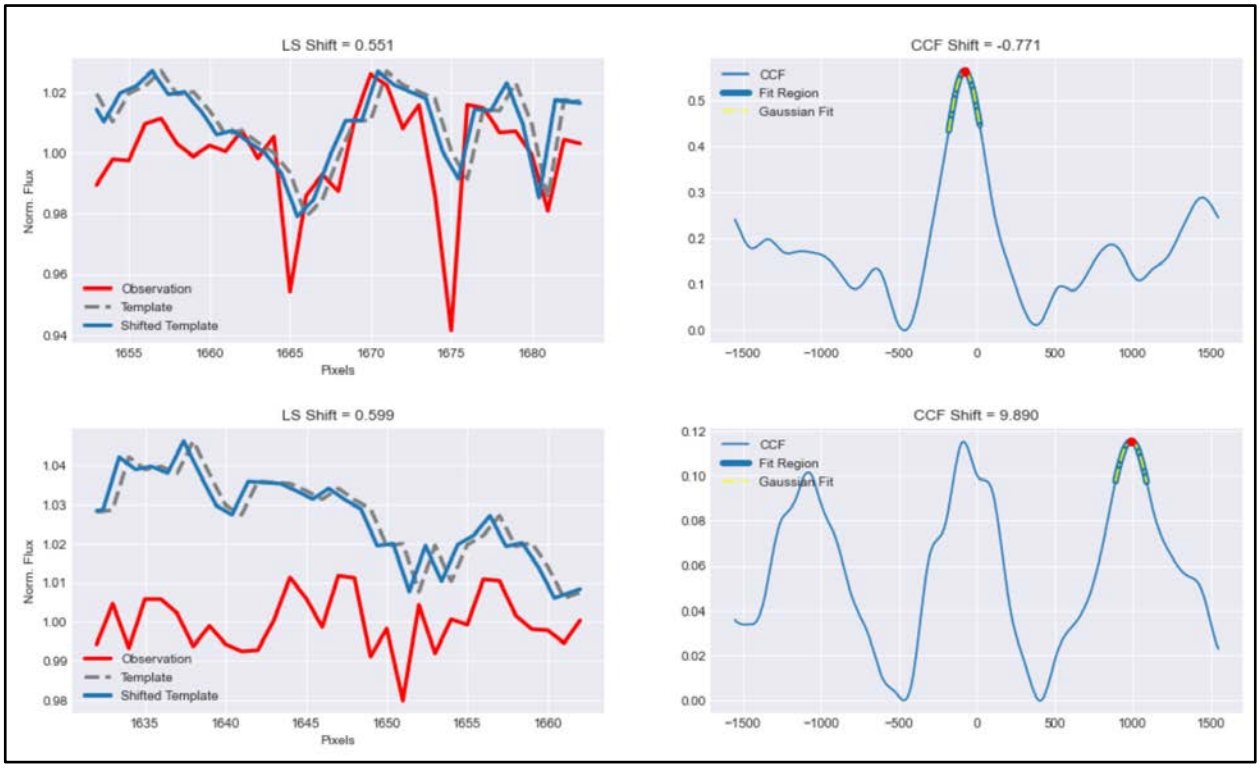

Figure 4. The cross correlation fits of two M dwarf spectrum chunks (red lines) with a 3000K model atmosphere (grey dashed line) were used to determine the pixel shifts between observations and an M dwarf template.

For spectral order 1, the wavelength values of the absorption features as a function of pixel position for all three stars were jointly fit with polynomials of orders 1, 2, and 4. The 4th order polynomial minimized the residuals without overfitting, as shown in Figure 5. The residuals of each fit function showed offsets between the wavelength values of the three stars. By adding offset corrections of 0.0004 and 0.0014 to the residuals of the A star and F star respectively (Figure 6), a joint wavelength solution was achieved with a residual scatter standard deviation of 44% of a pixel, below the 50% requirement stipulated in the activity's metrics for success. [2]

For spectral order 2, the wavelength values of the absorption features as a function of pixel position for all three stars were jointly fit with polynomials of orders 1, 2, and 4. The 4th order polynomial minimized the residuals without overfitting, as shown in Figure 7. The residuals of each fit function showed offsets between the wavelength values of the three stars. By adding offset corrections of 0.00025 and 0.0007 to the residuals of the A star and F star respectively (Figure 8), a joint wavelength solution was achieved with a residual scatter standard deviation of 42% of a pixel, below the 50% requirement.

For spectral order 3, the wavelength values of the absorption features as a function of pixel position for the A and F stars were jointly fit with polynomials of orders 1, 2, and 3. The order 3 trace for the M dwarf was too noisy to include in the solution. The 3rd order polynomial minimized the residuals without overfitting, as shown in Figure 9. The residuals of each fit function showed offsets between the wavelength values of the three stars. By adding an offset correction of 0.0003 to the residuals of the F star (Figure 10), a joint wavelength solution was achieved with a residual scatter standard deviation of 18% of a pixel, below the 50% requirement.

[2] https://outerspace.stsci.edu/display/NC/NAP-018

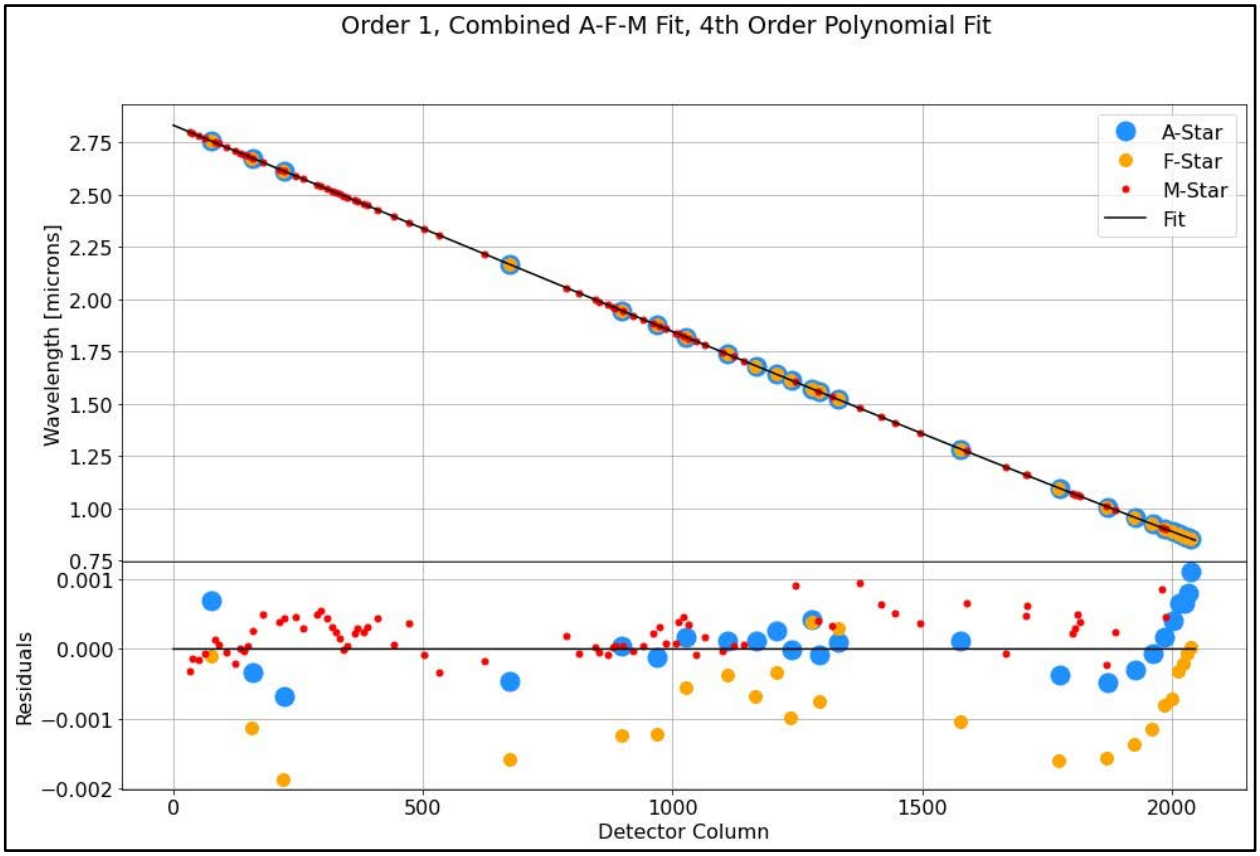

Figure 5. A 4th order polynomial fit (black line) to the A (blue), F (orange), and M (red) star order 1 absorption features as a function of detector pixel (top plot). The residuals (bottom plot) show an offset between the measured pixel positions for the three stars.

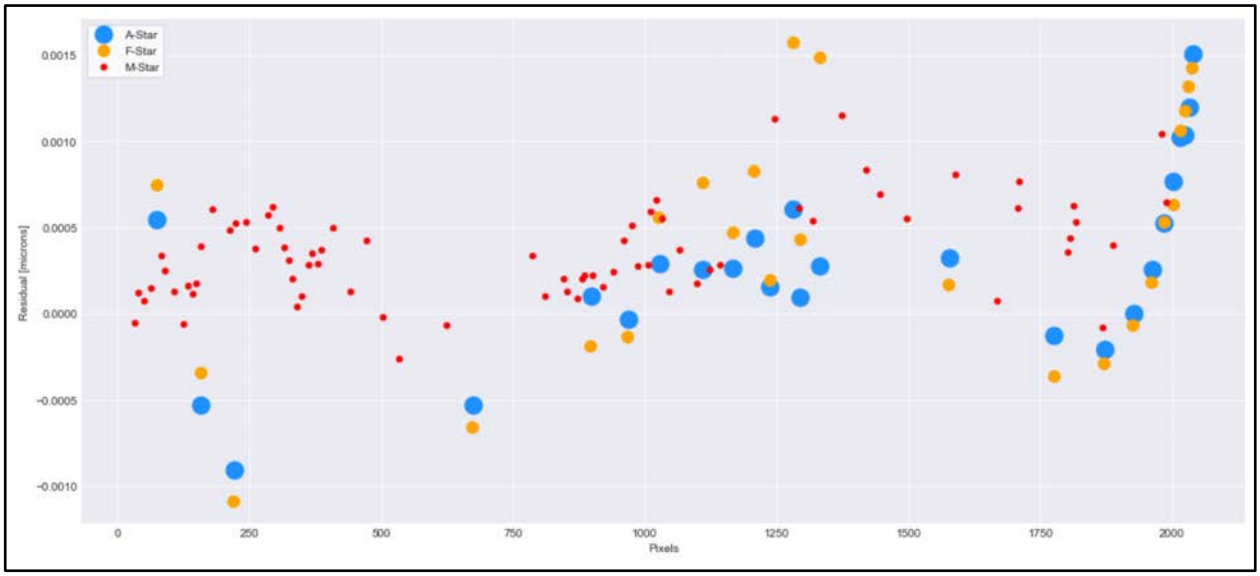

Figure 6. The residuals of the A (blue), F (orange), and M (red) order 1 absorption features as a function of detector pixel with offsets applied.

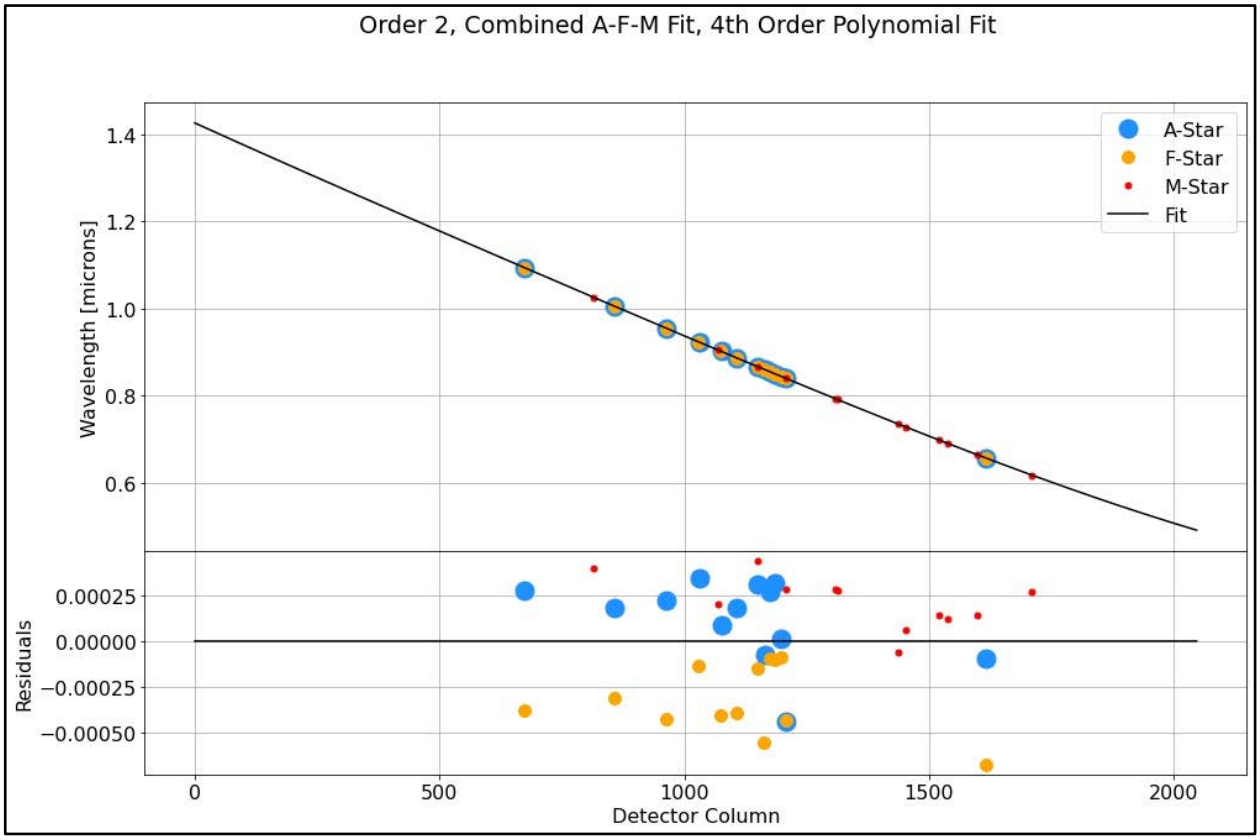

Figure 7. A 4th order polynomial fit (black line) to the A (blue), F (orange), and M (red) star order 2 absorption features as a function of detector pixel (top plot). The residuals (bottom plot) show an offset between the measured pixel positions for the three stars.

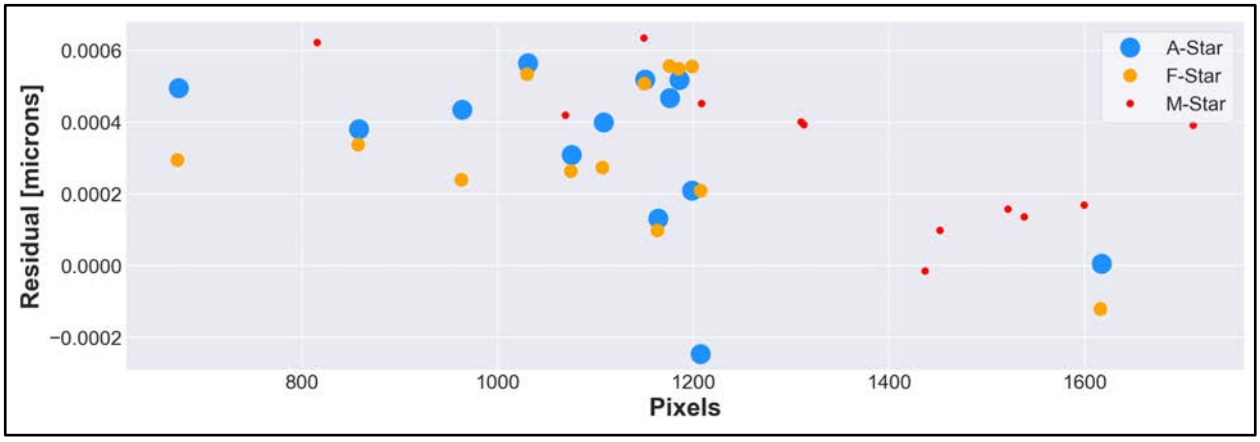

Figure 8. The residuals of the A (blue), F (orange), and M (red) order 2 absorption features as a function of detector pixel with offsets applied.

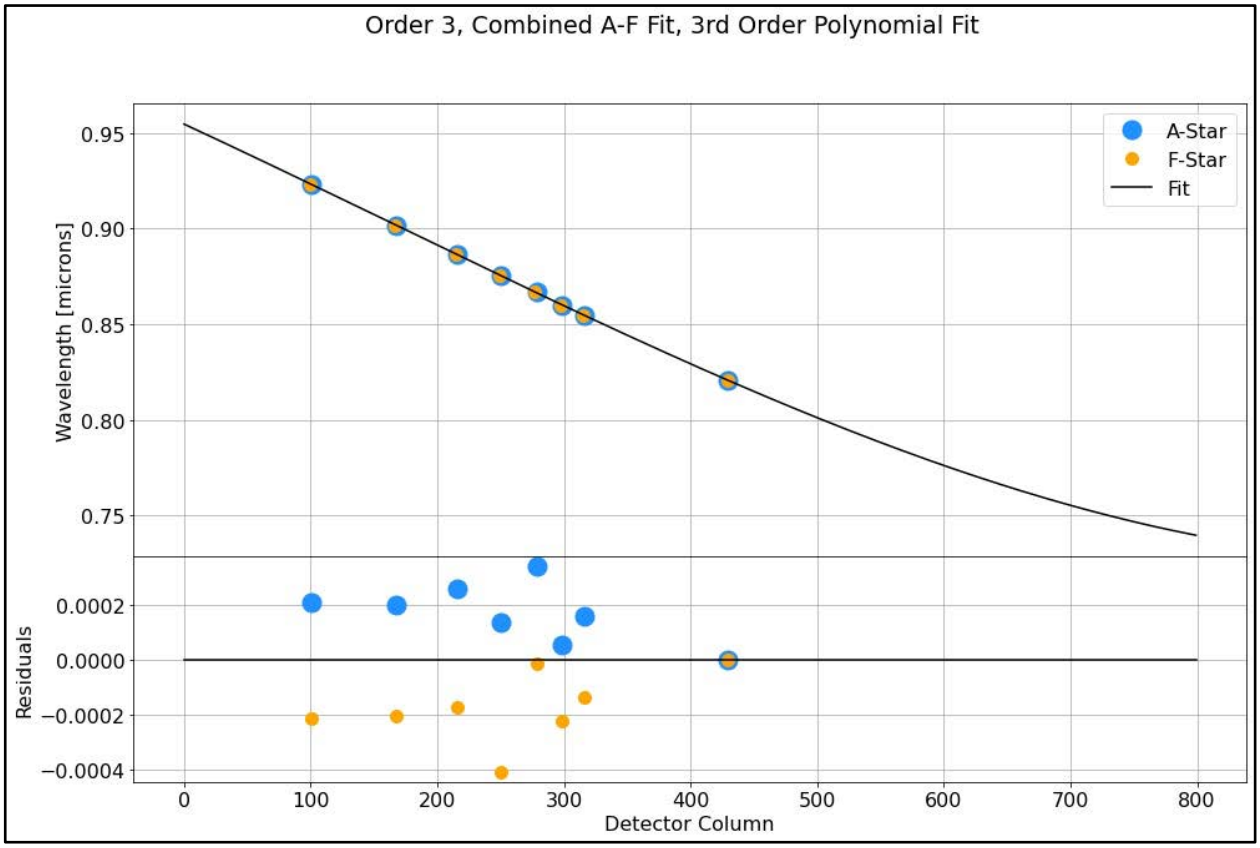

Figure 9. A 3rd order polynomial fit (black line) to the A (blue) and F (orange) star order 3 absorption features as a function of detector pixel (top plot). The residuals (bottom plot) show an offset between the measured pixel positions for the two stars.

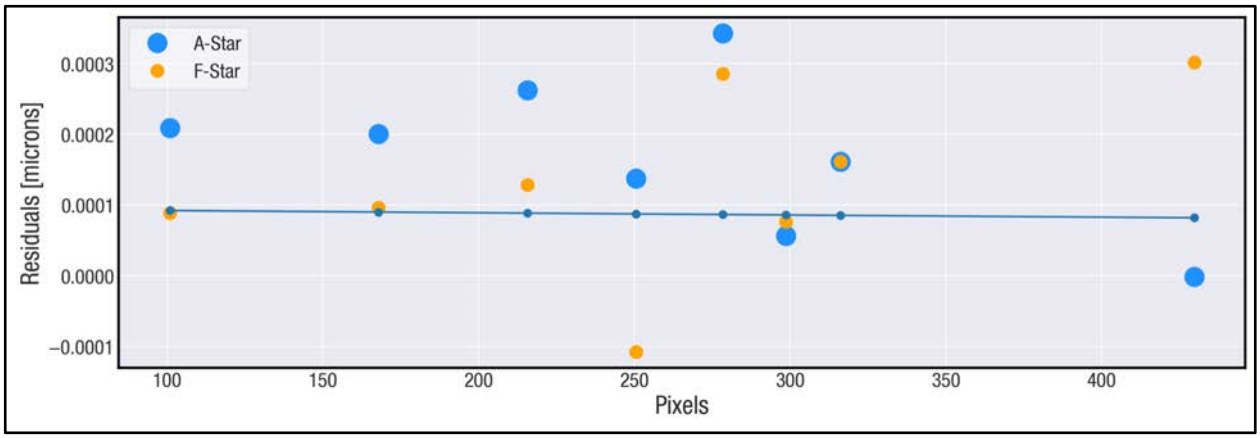

Figure 10. The residuals of the A (blue) and F (orange) order 3 absorption features as a function of detector pixel with offsets applied.

4.3. Wavelength Mapping and Reference Files

The nominal wavelength value at the center pixel of the trace was then projected in the cross-dispersion direction to assign a wavelength to each pixel on the detector for each order in the SUBSTRIP256 and SUBSTRIP96 subarrays as well as the FULL frame configuration.

To generate the 2D wavelength maps, the order 1, 2 and 3 trace positions from Section 4.1 and the 1D wavelength solutions determined in Section 4.2 were used. Together, these data give

pixel positions and wavelength values at the center of each trace in each of the 2048 detector columns. A 1D interpolation of the wavelength values was then used to assign a wavelength to each pixel.

The tilt of the 2D monochromatic PSF in each column is less than 1 degree according to tests of CV3 data and are not necessarily parallel with each other across the trace, meaning the wavelength values at the trace edges are slightly different than at the trace center in the same detector column. However, this tilt was set to 0 (perfectly vertical) for this analysis. Future wavelength calibrations will take this tilt into effect once it can be properly measured from on-sky data. This tilt did not affect the derivation of the 1D wavelength solution given the strength of the absorption features measured and the fitting routine employed. However, the reference files generated in this initial analysis do not reflect the true asymmetric nature of the wavelengths of light falling across the detector.

5. Data Products and Output

This commissioning activity generated data products in MAST up to Level2a for the M-dwarf observations. SOSS wavelength calibration reference file was produced, which contains a SUBSTRIP256 sized image with the wavelengths for each pixel in microns for orders 1, 2, and 3. Where no wavelengths are assigned the value is set to zero, these being pixels beyond the short wavelength ends of orders 2 and 3. All scripts used for analysis are available in a series of Python modules and Jupyter notebooks on Github (https://github.com/spacetelescope/niriss-commissioning).

6. Conclusions

The on-orbit wavelength solution as a function of detector pixel was measured for all three orders of the SOSS mode of NIRISS using observations of an A-type star, an F-type star, and an M-type star. Strong absorption features in each spectrum were used as anchor points for a wavelength solution for each spectral order.

Some discrepancies were seen among the residuals for the pixel positions of each star's absorption features, so offsets were applied and a joint solution was used. While the source of this disagreement is not known, a wavelength solution within the requirements was still achieved. A potential avenue of investigation into these discrepancies is the pupil wheel position during each observation, which may have altered the light path and shifted the trace position on the detector.

The 2D wavelength solutions assign a wavelength value to each pixel on the detector, however the observed tilt of the monochromatic PSF across the traces are not reflected in the output reference files pending further characterization of this effect.

References

Allard, F. et al. 2012, Philosophical Transactions A, 370, 1968.

Cushing, M.C., Rayner, J.T., Vacca, W.D. 2005, ApJ, 623, 1115.

Martel, A.R. 2019, Verification of the GSEG-3 Science Products, JWST-STScI-006878 (Baltimore: STScI)

Rayner, J.T., Cushing, M.C., Vacca, W.D. 2009, ApJS, 185, 289.

Reiners, A. et al. 2018, A&A, 612, A49.